

Article

Defect Estimation in Non-Destructive Testing of Composites by Ultrasonic Guided Waves and Image Processing

Kumar Anubhav Tiwari ^{1,2,*} , Renaldas Raisutis ^{1,3} , Olgirdas Tumsys ¹,
Armantas Ostreika ² , Kestutis Jankauskas ² and Julijus Jakutavicius ²

¹ Ultrasound Research Institute, Kaunas University of Technology, K. Baršausko St. 59, LT-51423 Kaunas, Lithuania; renaldas.raisutis@ktu.lt (R.R.); olgirdas.tumsys@ktu.lt (O.T.)

² Department of Multimedia Engineering, Kaunas University of Technology, Studentu g. 50, LT-51368 Kaunas, Lithuania; armantas.ostreika@ktu.lt (A.O.); kestutis.jankauskas@ktu.lt (K.J.); julius.jakutavicius@ktu.lt (J.J.)

³ Department of Electrical Power Systems, Faculty of Electrical and Electronics Engineering, Kaunas University of Technology, Studentu g. 50, LT-51368 Kaunas, Lithuania

* Correspondence: k.tiwari@ktu.lt; Tel.: +370-64694913

Received: 15 February 2019; Accepted: 8 March 2019; Published: 12 March 2019



Abstract: The estimation of the size and location of defects in multi-layered composite structures by ultrasonic non-destructive testing using guided waves has attracted the attention of researchers for the last few decades. Although extensive signal processing techniques are available, there are only a few studies available based on image processing of the ultrasonic B-scan image to extract the size and location of defects via the process of ultrasonic non-destructive testing. This work presents an image processing technique for ultrasonic B-scan images to improve the estimation of the location and size of disbond-type defects in glass fiber-reinforced plastic materials with 25-mm and 51-mm diameters. The sample is a segment of a wind turbine blade with a variable thickness ranging from 3 to 24 mm. The experiment is performed by using a low-frequency ultrasonic system and a pair of contact-type piezoceramic transducers kept apart by a 50-mm distance and embedded on a moving mechanical panel. The B-scan image acquired by the ultrasonic pitch-catch technique is denoised by utilizing features of two-dimensional discrete wavelet transform. Thereafter, the normalized pixel densities are compared along the scanned distance on the region of interest of the image, and a -3 dB threshold is applied to the locations and sizes the defects in the spatial domain.

Keywords: defect; composite; image processing; discrete wavelet transform; nondestructive testing; guided waves; glass fiber-reinforced plastic

1. Introduction

Composite structures made of glass fiber-reinforced plastic (GFRP) or carbon fiber-reinforced plastic (CFRP), such as a wind turbine blade (WTB) or a wing of an aircraft, are often subjected to cyclic loading, which leads to defects and delamination usually initiated at the microscopic or macroscopic level on the surface of the structure [1,2]. The detection of defects can be conducted by either of two ways: destructive or non-destructive testing (NDT). There are many non-destructive techniques; however, NDT using guided waves (GWs) has distinct advantages over other techniques. GWs are particularly useful for NDT and structural health monitoring (SHM) applications, because large areas can be interrogated with relatively few numbers of transducers [3–6]. Moreover, GW testing requires only minimal measurements to extract internal and surface defects in the large and complex composite structures [6–8].

Non-contact ultrasonic GW testing techniques can cover the large surface area of the object being investigated. However, they have certain limitations due to the layered structures, thick size, and low acoustic contact between the transducers and contact surface [9]. On another hand, in the field of contact ultrasonic testing, most of the research and commercial testing of WTBs has been performed by either pulse-echo technique (the same transducer operates as a transmitter and a receiver) [10,11] and ultrasonic phased array (many transducers are connected to form an array) [12,13]. The real-time testing of WTB is quite challenging because of its composite and thick structure and the possibility of only one-sided access. Hence, more research is required in this field [14]. Moreover, there are some limitations associated with pulse-echo and ultrasonic phased array techniques. The pulse-echo technique is less flexible and unsuitable for large structures, and the phased array method is expensive and complex due to the added number of devices. This provides the motivation to develop measurement techniques based on a pitch-catch operation by only using two transducers, which is more flexible as compared with the pulse-echo technique and more economical as compared with the phased array method. However, the experimental data and results are not enough to identify the location and size of the defects. The experimental data must be processed either by signal processing or image processing techniques.

The objective of this work is to estimate the size and location of disbond-type defects located on a GFRP sample possessing a variable thickness by using ultrasonic GWs and an image processing technique. A mechanical machining process was used to create defects. The experiment was performed with a low-frequency (LF) ultrasonic system and a pair of similar piezoceramic ultrasonic transducers operating in a pitch-catch mode. The transducers are very sensitive to the amplitude (pixel density in the context of the image) variations of *out-of-plane* waves. In the first experiment, the dispersion curve was acquired in order to show the dominant A0 mode. Afterward, linear scanning was performed over the defective regions to acquire the B-scan image. In the next step, image denoising was performed by using two-dimensional discrete wavelet transform (2D-DWT). Afterward, the region of interest (ROI) was selected in such a way that faster modes of guided ultrasonic waves interacted more intensively with the defective region. The normalized pixel densities along the scanned distance were then estimated, and the application of a -3 dB threshold provided information about the location and size of the defects.

2. Background

2.1. Guided Wave Propagation in Composite Structures

Prior studies provided evidence of the utilization of GWs to estimate damages and defects in various structures, including pipes [15–17], concrete structures [18,19], metals [20], and composite structures [21–27]. However, the interaction of GWs with multi-layered composite materials such as GFRP and CFRP may lead to the scattering, reflection, mode conversion, etc. of GWs. Although the detection of defects is possible by experimental scanning, identifying the size and location of defects requires the post-processing of experimental results. The possible mechanisms that may occur during the interaction of ultrasonic GWs with the layered structure of composites are reflection or refraction of wave modes, scattering, and mode conversions. This increases the complexity of the received ultrasonic signals, so that the extraction of defect-related information becomes very difficult. Hence, the post-processing of experimental results is required for the estimation of the size and location of defects in composite material.

2.2. Image Processing Technique

The post-processing of GW signals becomes even more critical in the case of a B-scan image, which has significantly much less information as compared with the conventional C-scan image. Either a signal processing or image processing approach can be applied to improve the accuracy in the measurement. Many signal processing techniques have been used for the refinement of experimental results by analyzing the amplitudes, phase velocity, instantaneous frequencies, or time of flight of the received signals [4,28–32]. However, the consideration of the experimental results as an image requires an effective image processing

technique to extract the defect features. An image processing technique in ultrasonic testing is used to denoise the image in order to extract the information about the presented defects. On the basis of prior studies, the image processing and denoising methods in the field of ultrasonic NDT of composite structures include image correlation, 2D-DWT, two-dimensional empirical mode decomposition (2D-EMD), two-dimensional variational mode decomposition (2D-VMD), etc. [33–36]. Apart from other parameters, the selection of image processing for the estimation of the size and location of defects from a B-scan highly depends on the type of transducers, variations in the pixel densities along the scanned distance, and the size of the defect.

There are many transformation techniques available for denoising an image, including Wiener filter processing, median filter, mode decomposing techniques such as EMD and VMD, etc. However, DWT has certain advantages as compared with short-time Fourier transform (STFT) and mode decomposition techniques in terms of variable window size [32,37]. Moreover, DWT provides temporal information in addition to amplitude and frequency information, which is lost in other transformations [38].

DWT subsequently reduces granular and structural noise from ultrasonic B-scans acquired by ultrasonic NDT of composite structures [39–41]. In the process of DWT, the signal-to-noise ratio (SNR) is improved, which, in turn, increases the probability of identifying the location and size of the defects. The decomposed signals are called wavelets, and wavelet transform is the correlation between the time-domain signal and the elementary wavelets. The basic principle of wavelet denoising depends on signal preservation by reducing the smaller amplitude components irrespective of frequency. By altering the wavelet coefficients, denoising can be achieved [42,43]. Image transformation from the spatial domain to the frequency domain using DWT is performed by hierarchical functions [44].

In order to denoise an image, 2D-DWT is performed, which includes the application of one-dimensional DWT in sequence along the rows and columns respectively [45]. In single dimensional DWT (1D-DWT), there is one L sub-band and one H sub-band corresponding to the low-pass filter (LPF) and high-pass filter (HPF), respectively. Decomposition using 2D-DWT can be described as follows:

- There will be four sub-bands LL , LH , HL , and HH in the wavelet domain after one level of 2D decomposition.
- After convolving the LPF in both directions (horizontal and vertical), the LL sub-band is generated, which basically represents the approximated image.
- After convolving the LPF in the horizontal direction and the HPF in the vertical direction, the LH sub-band is produced, which, in general, represents the vertical characteristics of an original image.
- The HL sub-band represents the horizontal characteristics of the image. It is generated by the reverse process of that performed to produce the LH sub-band. Hence, convolving the HPF in the vertical direction and convolving the LPF in the horizontal direction is performed.
- After convolving the HPF in both directions (horizontal and vertical), the HH sub-band is generated, which basically represents the diagonal edge characteristics of the image.
- The noise is mostly concentrated in the HH sub-band, while the LL sub-band contains most of the image features.

The process is repeated depending on the number of decomposition levels.

If M is the maximum level of decomposition, the k th level of decomposition can have any value between 1 and M and can be expressed by following Equation (1) [46]:

$$M = \log_2 N \quad (1)$$

where N is the length of original signal $x[n]$.

The soft threshold technique with a universal threshold is widely used for manipulating the wavelet coefficients, especially in the presence of correlated noise [47]. The appropriate noise threshold, using a universal threshold for the detailed components, can be expressed as follows [46]:

$$\lambda = \sigma_j^{\text{noise}} \sqrt{2 \log(N)} \quad (2)$$

where σ_j^{noise} is the estimated noise level.

There are different mother wavelets or wavelet families. However, Daubechies (db) wavelet, due to orthogonality in nature and energy preserving capabilities, is preferred here [30,48]. After denoising by discarding the wavelet coefficients using an appropriate threshold, inverse 2D-DWT (2D-IDWT) is performed to reconstruct the denoised B-scan image. In order to distinguish between defect-free and defective regions, an amplitude detection (pixel densities in context of the image) technique is generally applied with an appropriate decision level to distinguish between the amplitude/pixel variations [37]. In this way, the approximate size and location of the defects can be estimated.

3. Experimental Analysis

3.1. Object of Investigation

A segment of WTB constructed from GFRP was considered here. The schematic of the WTB segment and a photo of the sample containing a disbond of 25 mm on the inner side of the main spar are shown in Figure 1.

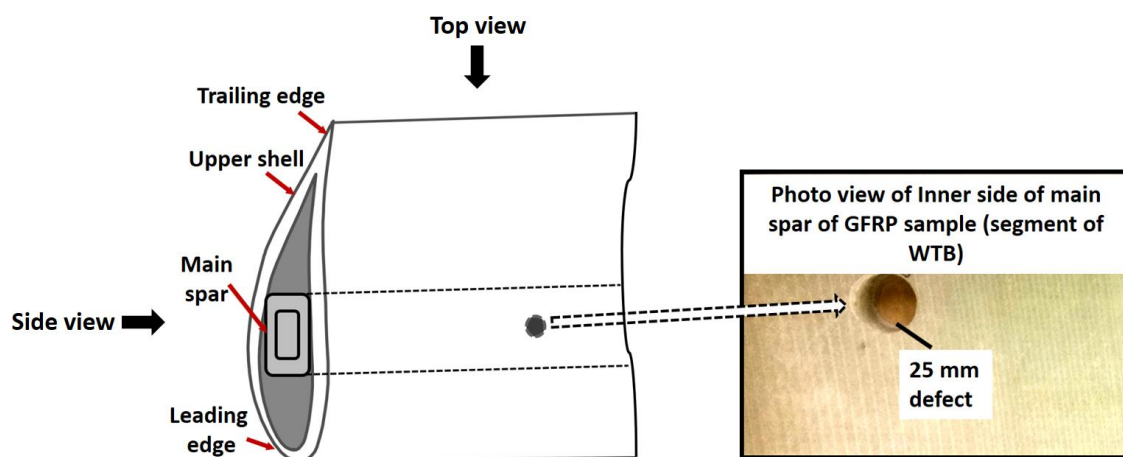


Figure 1. Showing a schematic of a typical segment of a wind turbine blade (WTB) and a photo view of the inner side of the sample containing a disbond of 25-mm diameter. GFRP: glass fiber-reinforced plastic.

The defect was created artificially by using a mechanical technique called a milling method. The sample of WTB had variable thickness in the region without defects, as well as in that with defects. The thickness of the sample was in the range of 20–23 mm in the region of no defects, whereas it was 3–5 mm in the region containing a defect with a 25-mm diameter. The defect was not visible during the experimental analysis, because the scanning of the ultrasonic transducers was performed on the other (outer) side of the sample.

3.2. Devices and Experimental Set-up

Point-type contact ultrasonic transducers constructed from piezoceramic (Pz29) were used in the experiments. The characteristics of transducer are presented as follows [38,49]:

- The center frequency of transducers was 190 kHz.
- The –6 dB bandwidth was up to 250 kHz.
- The –10 dB bandwidth was in the range from 35 kHz to 640 kHz.
- The diameter of the conical-shaped protection layer equipped at the bottom of the transducer was 0.2 mm.

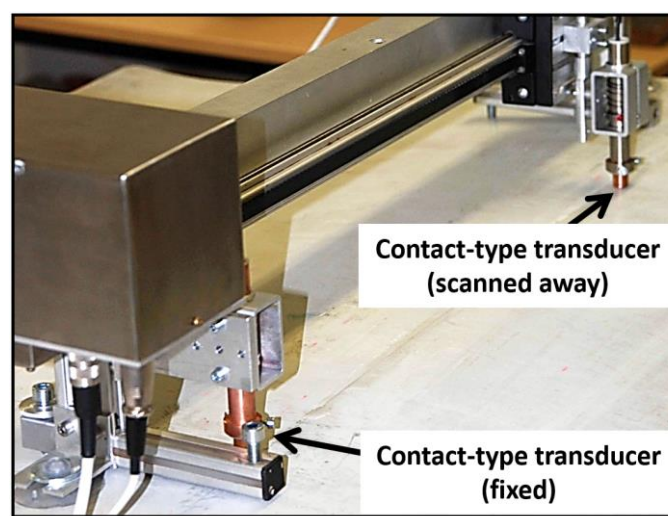
The LF ultrasonic system “*Ultralab*” was used in this research to perform the experiment. All the components, including the transducers and the LF ultrasonic system, was developed at the Ultrasound Research Institute of Kaunas University of Technology. The characteristics of the LF ultrasonic system are presented in Table 1 [31,32,37].

Table 1. Characteristics of the LF ultrasonic system “*Ultralab*”.

Parameters	Numerical Value
Number of channels	2
Number of bits of the analog-to-digital converter	10
Frequency range	20 kHz–2 MHz
Maximum system gain	113 dB
Resolution of the mechanical scanner	20 μm
The interface between the system and computer	USB V.2

Before inspecting the sample for the analysis of defects, a linear scanning in the defect-free region was performed to estimate the dispersion curve. One contact type transducer was kept fixed and excited by 250 V, 150 kHz, and a 3-period burst-type signal, while another transducer was scanned away up to 200 mm with a scanning step of 1 mm to record the GW signals. Glycerol was used as a coupling liquid to maintain the acoustic contact between the sample and the transducers. A photo view of the experiment is presented in Figure 2a, and the acquired B-scan is shown in Figure 2b. In the ultrasonic NDT, two-dimensional fast Fourier Transform (2D-FFT) is used to transform the B-scan (time–distance measurements) into the phase the velocity–frequency domain [30,32,50]. The basic principle of 2D-FFT is the representation of GW propagation by the transfer function (H) of arrival time and scanning distance. This in turn is transformed into the frequency (f) – wavenumber (k) space [51,52], and therefore, the phase velocity characteristics can be obtained along the frequency. The dispersion curve is presented in Figure 2c.

Both contact-type transducers are very sensitive to pick up A_0 mode, and that is why the dominant A_0 mode is clearly observed in Figure 2c with a phase velocity of 1160 m/s at 150 kHz excitation frequency. Therefore, for further investigation of such a sample, A_0 mode will be the interesting mode of consideration when using the same contact-type transducers. The wavelength of A_0 mode at 150 kHz was 7.73 mm.



(a)

Figure 2. *Cont.*

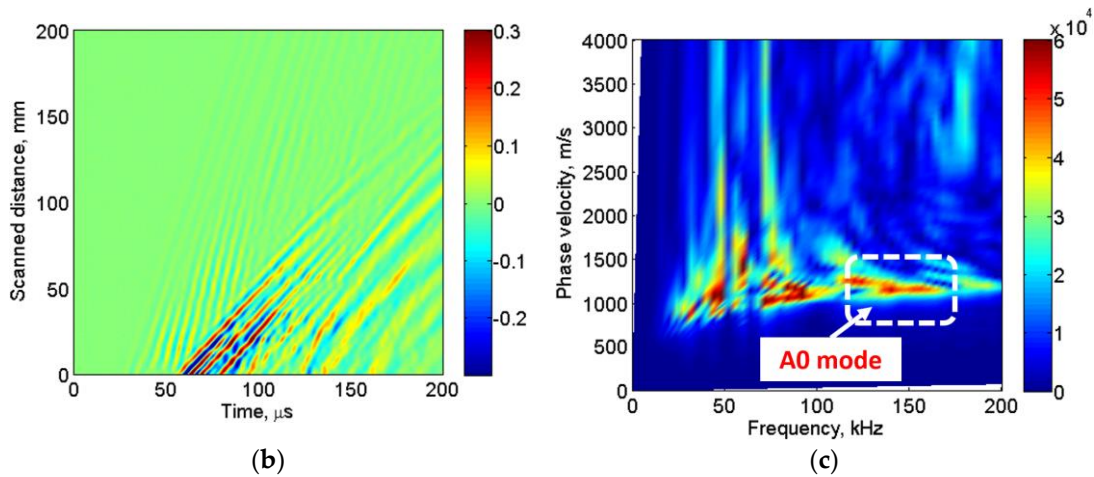


Figure 2. Estimation of dispersion curve: (a) photo view of the experiment, performing linear scanning in the defect-free region; (b) B-scan image; and (c) dispersion curve after the application of two-dimensional fast Fourier Transform (2D-FFT).

In the next experiment, scanning over the defective regions was performed. The schematic of the experimental set-up with the LF ultrasonic system, location of transducers, and 25-mm disbond-type defect is presented in Figure 3. During the entire experiment, the defect was not visible, as the experiment was performed on the outer side of the sample. The scanning was performed across the surface, and it covered the region of the leading edge, main spar, and trailing edge of the WTB. Therefore, the thickness of the multi-layered material varied from 3 to 23 mm, which added more complexity to the estimation of the defects. However, the defect itself was located on the main spar of the sample (segment of the WTB), and the thickness of the structure in the defective region was between 3 and 5 mm.

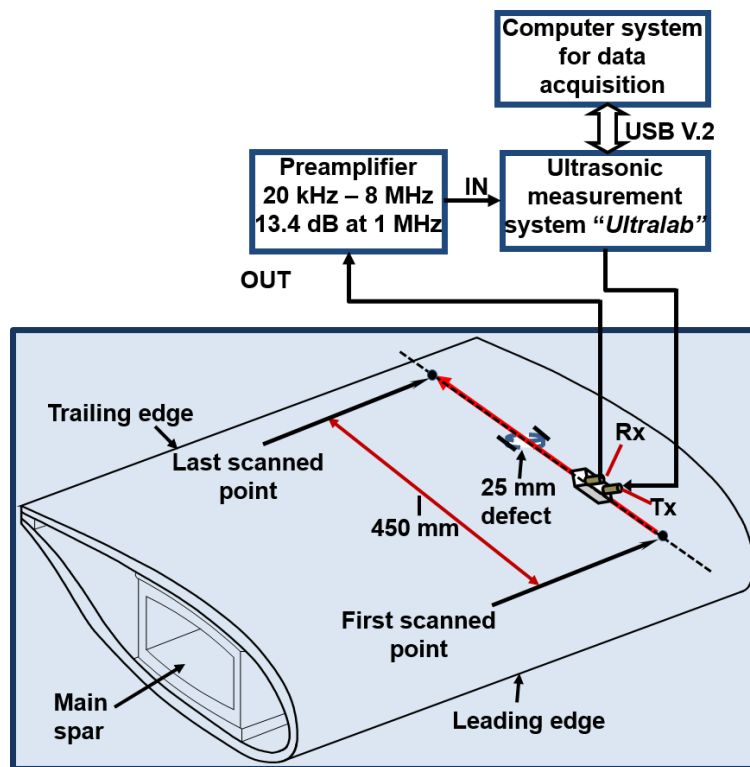


Figure 3. Experimental set-up showing the connection of transducers with the LF ultrasonic system for linear scanning over the defective regions.

A pair of ultrasonic contact-type piezoceramic transducers, as used in the previous experiment (see Figure 2a), was used as a transmitter–receiver to scan the sample. However, in this experiment, both transducers were mounted on a mechanical unit and separated by an optimal distance of 50 mm. The transducers operated in thickness mode and, thus, were more sensitive to transmit/generate the out-of-plane asymmetric (A0) guided waves possessing the dominant out-of-plane component. The distance of 50 mm ensured the required resolution, and it was selected to be equal for the few wavelengths of the A0 mode. The wavelength (λ) of the dominant A0 mode was 7.73 mm at the excitation frequency of 150 kHz. That is why the separation distance of 50 mm (approximately equal to 7λ) was selected.

Possible effects due to wave interference and cross-talk were prevented by insulating both transducers from the casing of the holder. As this technique depends on the amplitude variations, the constant contact pressure had to be maintained throughout the scanning process. The contact pressure was kept constant by using spring-type holders of the transducers.

The schematic and photo view of the pair (transmitter–receiver) of transducers are shown in Figure 4a,b. The transmitter was excited by 250 V, 150 kHz, and a 3-period burst-type signal with Gaussian symmetry, and the receiver recorded the guided wave signals at each 1 mm up to the scanning distance of 450 mm. The distance between the initial scanned point and the nearest edge of the defect was 215 mm. The B-scan image along the spatial range (0–450 mm) and time (0–400 μ s) is presented in Figure 5. It is also observed that the defect-free region is noisier in the spatial range (0–200 mm) as compared with that in the spatial range (250–450 mm). The reason behind this is that the thickness of the multi-layered structure varied from 23 mm up to 3 mm during the scanning. A thicker and more complex segment of layered structure produces mode conversions, scattering, reflections, and generation of higher order modes.

As transducers are more sensitive to out-of-plane A0 waves, the scattered, reflected, and mode-converted guided waves possessing the dominant out-of-plane component can be clearly observed in the region of defect. In our previous works with the similar kind of transducers, it was already observed that the amplitude of the dominant A0 component of the propagating GW decreased significantly in the region of defects due to one of the possible wave mechanisms (e.g., dispersion, scattering, reflection, mode conversion, etc. [10,24,53]). Hence, the detection of the defective region is possible in the B-scan image (Figure 5). However, the estimation of size, location, and characterization of the defect-free and defective regions of structure require the processing of the experimental B-scan image. As discussed in Section 1, image processing techniques were used to extract the defect features.

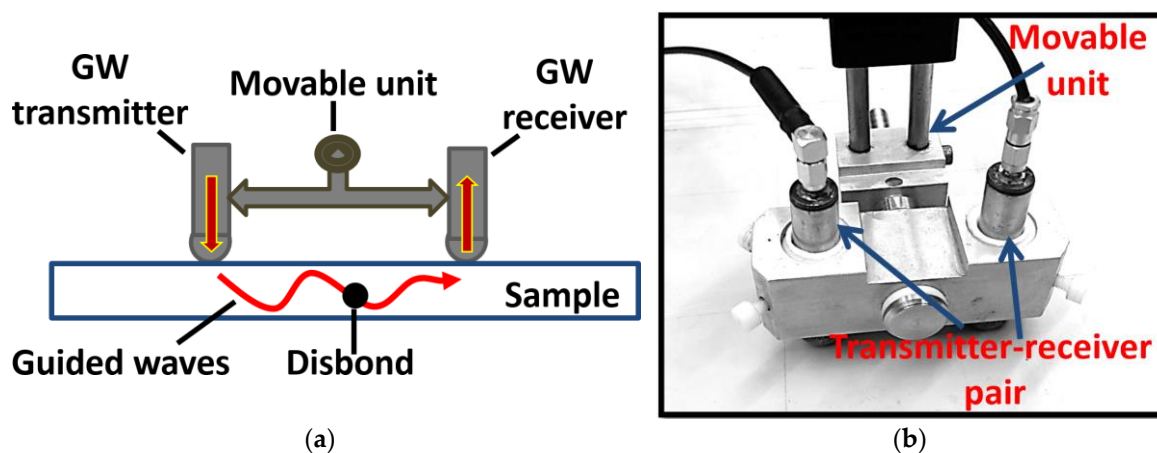


Figure 4. Showing (a) a schematic of the arrangement of transducers (transmitter–receiver pair) on a moving panel and (b) a photo view of transducers. GW: guided waves.

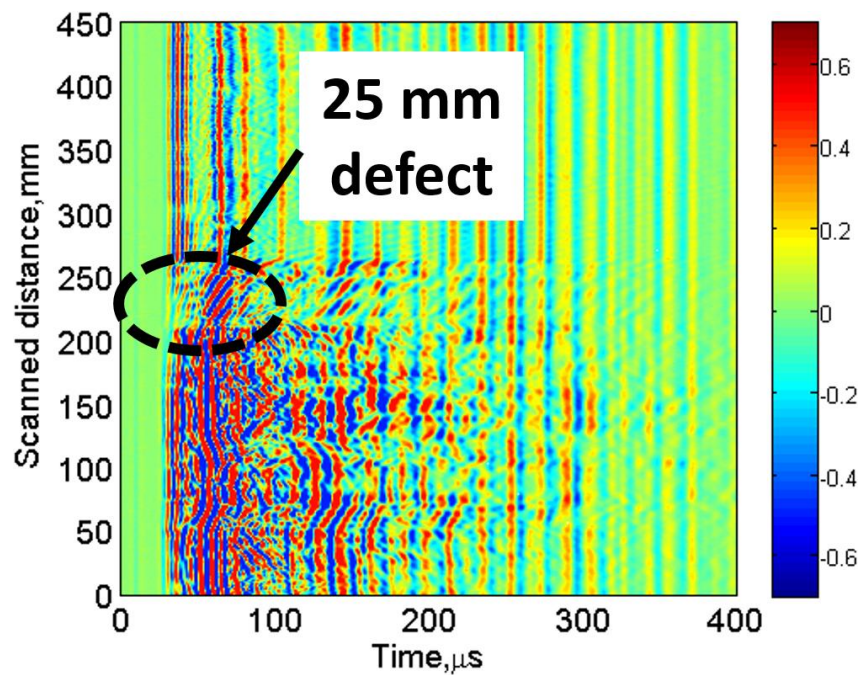


Figure 5. Acquired B-scan image after scanning over the 25-mm disbond-type defective region.

4. Results and Discussions

The image processing of the experimental B-scan requires pre-processing, image denoising, and the extraction of defect features from the denoised image. The image processing technique utilized in this work is presented in Figure 6.

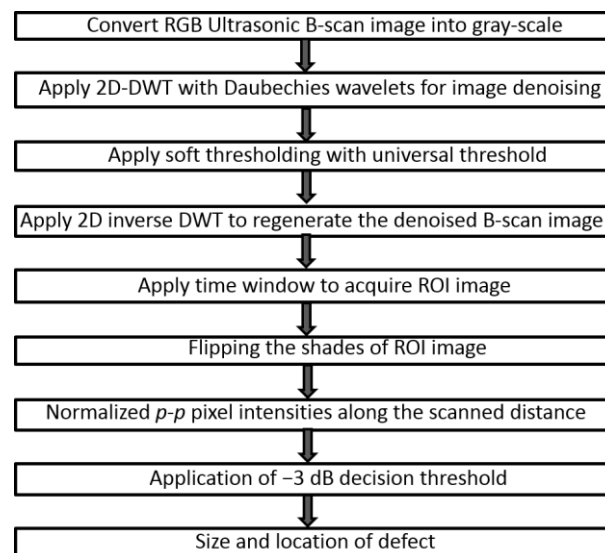


Figure 6. Descriptive flow chart showing the sequential steps of the image processing of the B-scan image. RGB: red, green and blue; 2D-DWT: two-dimensional discrete wavelet transform; ROI: region of interest; and p-p: peak-to-peak.

The sequential steps performed in the process are as follows:

- The first step involves preprocessing the acquired B-scan image from the experiment. The preprocessing of the image is required to convert the image into the compatible format for the denoising. Most of the image denoising processes and transformations work better for

a gray-scale image as compared with an RGB image (Figure 4b). Hence the RGB image of the B-scan was converted into a gray-scale image, as shown in Figure 7a.

- The contact-type transducers operate in thickness mode, which is more sensitive to the amplitude variations along the scanned distance. Concerning the image processing, the variations in the orientation and densities of the pixels would be a key factor in the process of estimating the size and location of the defect. The considerable amount of changes in the pixel densities could lead to identifying the location and size of the defect. However, before proceeding to the defect estimation, the first step is to denoise the image in order to remove the structural and non-stationary noise from the B-scan image. As discussed in Section 2, the eight-level decomposition with db8 mother wavelet of DWT and soft threshold with a universal threshold is used for denoising the image. The denoised image after the application of inverse 2D-IDWT is shown in Figure 7b.
- In the next step, the region of interest of the image (ROI) is selected by applying the appropriate time window of (0–55 μ s) to the denoised image. The selection of the specific time window was on the basis of intensive interaction of the GWs with the defect in this time interval. The denoised ROI image is presented in Figure 7c.
- The pixel values of the ROI image are normalized between 0 and 1. The image is regenerated and shown in Figure 7d.
- In the last step, the shades of the image (Figure 7d) are flipped for the final processing. The image generated by flipping the shades is shown in Figure 7e.

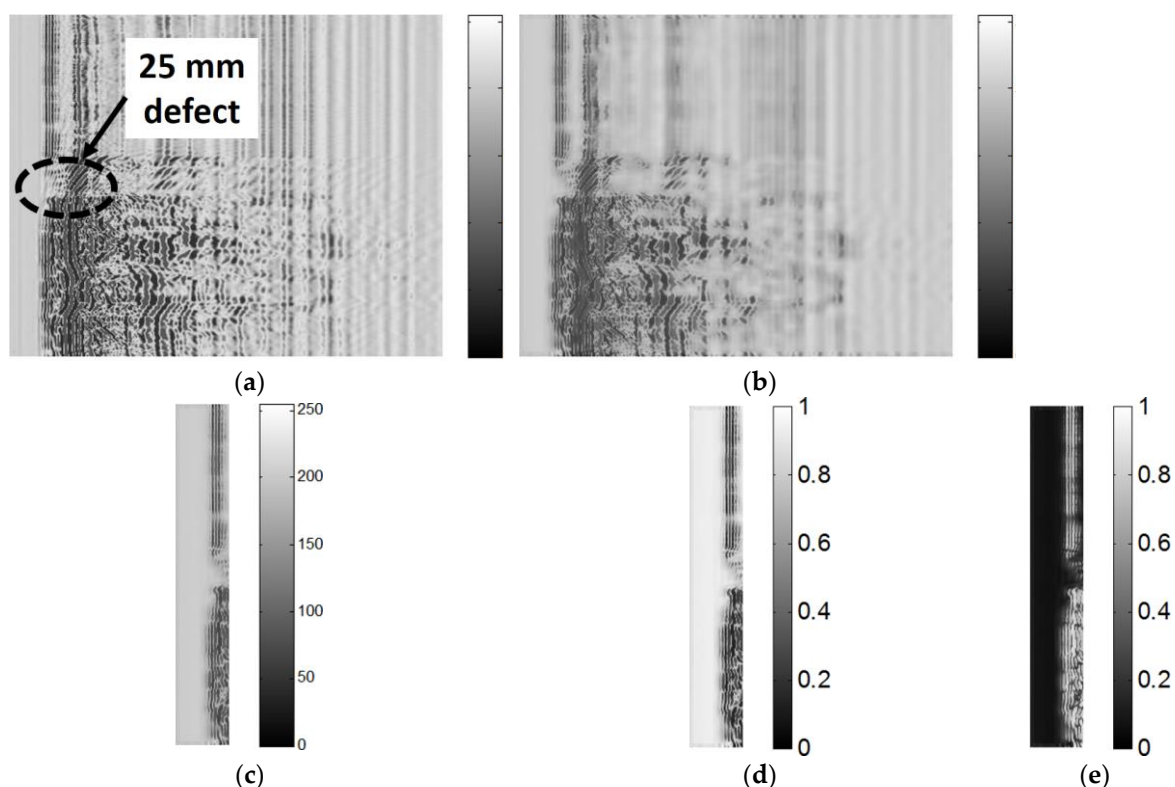


Figure 7. The image processing of the B-scan image: (a) Gray-scale image of the experimental B-scan; (b) denoised image after processing by 2D-DWT; (c) ROI image after applying the time window on the denoised image; (d) regenerated ROI image by normalizing the pixel values between 0 and 1; and (e) image generated by flipping the shades of the image (inverting the pixel values).

In order to estimate the size and location of the 25 mm defect, the peak-to-peak (p-p) normalized pixel intensities of the image (Figure 6e) along the scanned distance (0–450 mm) was obtained and is presented in Figure 8. In ultrasonic NDT, the decision level (−3 dB) is very common, especially for the

comparison of amplitudes of propagating waves [37,54]. By selecting the -3 dB threshold, the detection of the defect is clearly visible. The size and location of the 25 mm defect are measured as 34 mm and 205 mm, respectively. Subsequently, the relative errors in the estimation of the size and location are 36 and 4.65%, respectively. Although the accuracy in the size of the defect is significantly higher, the accuracy in the estimation of the location of the defect is low. There are many factors that may limit the accuracy of estimating the size and location of the defect by using the presented methodology:

- This technique is not suitable to estimate microcracks, because the linear ultrasonic technique used in this research is valid if the diameter of the defects is more than the operating wavelength. Non-linear scanning techniques [55,56], which are very sensitive to the microcracks, can be an alternative for smaller defects.
- The optimal distance between the two transducers (50 mm) is greater than the size of the defect (25 mm), which is one of the major limiting factors to estimate the size of the defect. However, the optimal distance depends on the transducer bandwidth and wavelength of the slowest (A0) mode. The lower value of the optimal distance (closer to the size of the defect) may increase the accuracy in measurement.
- The pixel intensity (amplitude)-based approach is very sensitive to the environmental and operating conditions. Therefore, a constant temperature of 25 °C has been maintained during the experimental process.

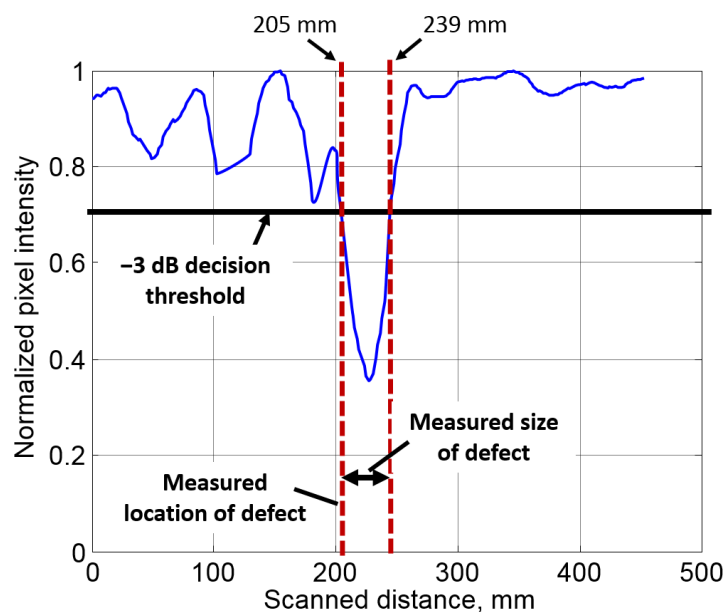


Figure 8. Normalized pixel intensity distribution along the scanned distance.

Estimation of the Defect Having a Size Greater than Optimal Distance (50 mm) of Transducers

In order to validate the technique and understand the effect of the optimal distance (50 mm) between the traducers on the accuracy of the defect estimation, the defect having a diameter of 51 mm (greater than the optimal distance between the transducers) located on the GFRP sample was investigated by the same experimental set-up. In comparison with the variable thickness of the structure during the scanning of the 25 mm defect, the thickness in this case was almost similar (10–12 mm). The true location of the 51 mm defect was at 82 mm from the initial scanned point. The parameters of the excitation signal and sampling frequency were similar to those used in previous experiments for the investigation of 25 mm defects. The B-scan was acquired after scanning over the defective and defect-free regions up to 180 mm. Figure 9 presents the B-scan image along the spatial range of 0–180 mm and time range of 0–200 μ s.

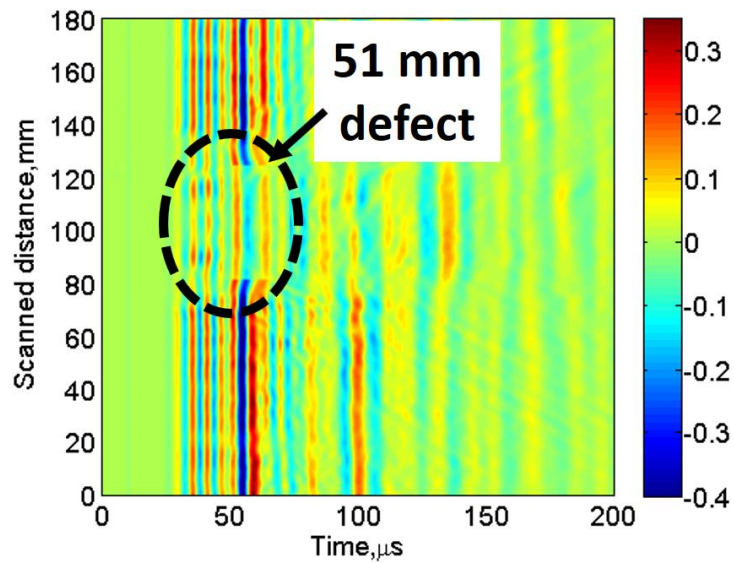


Figure 9. Acquired B-scan image after scanning over the 51-mm defective region.

In the next step, the image processing technique as described in Figure 4 was applied in sequence on the B-scan image. The results of image processing technique (image denoising and ROI image) are presented in Figure 10a–e.

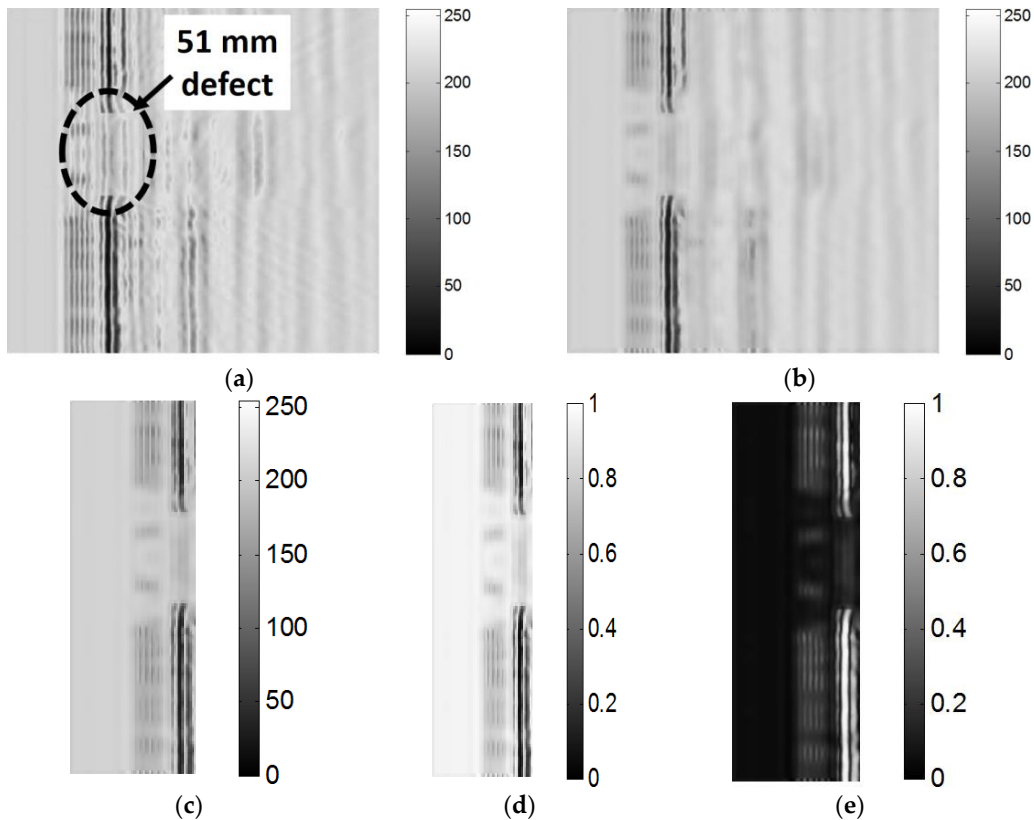


Figure 10. Image processing of the B-scan image in the case of the 51-mm defect: (a) Gray-scale image of the experimental B-scan; (b) denoised image after processing by 2D-DWT; (c) ROI image after applying the time window on the denoised image; (d) regenerated ROI image by normalizing the pixel values between 0 and 1; and (e) image generated by flipping the shades of the image (inverting the pixel values).

The p - p pixel densities of the final normalized ROI image (Figure 10e) were estimated. The normalized p - p pixel density variations along the scanned distance (0–180 mm) are presented in Figure 11. The threshold of -3 dB was applied in order to estimate the size and location of the 51-mm defect. The estimated size and location of the 51-mm defect were 53 mm and 80.5 mm, respectively, with respective relative errors of 3.9 and 1.8%. Hence, the accuracy in the results was higher as compared with the estimation of the 25-mm defect. This confirms that the accuracy of the results also depends on the optimal distance between the transducers apart from the operational frequency, type of transducers, etc.

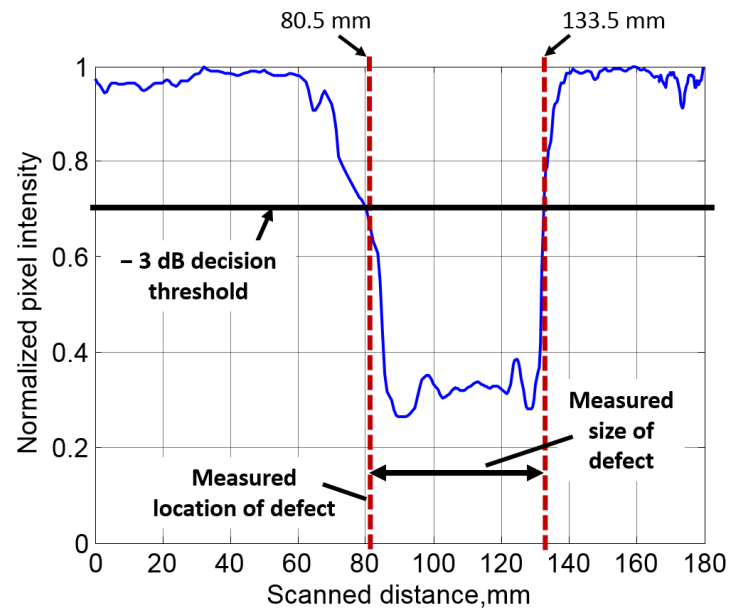


Figure 11. Normalized pixel intensity distribution along the scanned distance in the case of the 51-mm defect.

The comparative results in the estimation of the size and location of both the 25- and 51-mm defects are presented in Table 2.

Table 2. Analysis of results.

Parameters	True Value, mm	Measured Value, mm	Relative Error, %
Location of 25 mm defect	215	205	4.65
Location of 51 mm defect	80.5	80.5	1.83
Size of 25 mm defect	25	34	36
Size of 51 mm defect	51	53	3.9

5. Conclusions

Most of the scientific research and commercial testing of composite structures possessing an aerodynamic shape has been performed by ultrasonic pulse-echo and phased array methods. In this paper, we have demonstrated the feasibility of an ultrasonic pitch-catch technique incorporated with image denoising and an image processing technique that allows the detection and estimation of disbond-type defects in a multi-layered GFRP composite structure possessing an aerodynamic shape. The conclusions of this work can be summarized as follows:

- During the experiment, a pair of contact-type piezoceramic transducers fixed on a moving mechanical panel with a separation of 50 mm was used. This reduced the attenuation losses due to the longer distance between the transmitter and receiver during the scanning process.

- The detection of defects from the experimental B-scan image was possible with significant accuracy. The estimation of the size and location of the defects required the post-processing of the B-scan image.
- The B-scan image is denoised and processed in order to estimate the normalized pixel intensity distribution along the scanned distance. This subsequently allows for the analysis of the location and size of the 25 mm and 51 mm defects located on the main spar of the GFRP sample, which was a segment of a wind turbine blade.
- Higher accuracy was achieved in the case of the 51-mm defect, which allowed us to conclude that the accuracy of the defect estimation of the proposed technique depends on the optimal distance between the transducers. The other factors that limit the accuracy of measurement of this technique are also discussed in detail.
- Incorporating this technique into automatic ultrasonic measurement systems will help make a reliable decision about internal defects. It also provides the motivation for the development of a transducer pair with the minimum possible optimal distance for the estimation of small-sized defects.

In the future, studies investigating minimizing the limiting factors and incorporating signal processing techniques with image processing methods are needed.

Author Contributions: Conceptualization, K.A.T. and R.R.; methodology, K.A.T. and R.R.; software, K.A.T. and J.J.; validation, K.A.T. and R.R.; formal analysis, A.O. and K.J.; investigation, K.A.T.; resources, O.T., A.O., J.J. and K.J.; data curation, O.T. and J.J.; original draft preparation, K.A.T.; review and editing of manuscript, K.A.T. and R.R.; visualization, K.A.T., O.T. and A.O.; supervision, R.R., O.T. and A.O.; and project administration, R.R. and K.J.

Funding: This research received no external funding.

Acknowledgments: This work was performed via the joint efforts of an interdisciplinary research team from Kaunas University of Technology, Lithuania.

Conflicts of Interest: The authors declare no conflict of interest.

References

1. Mrazova, M. Advanced composite materials of the future in aerospace industry. *INCAS Bull.* **2013**, *5*, 139–150.
2. Xu, B.; Li, H.Y. *Advanced Composite Materials and Manufacturing Engineering: Selected Peer Reviewed Papers from the 2012 International Conference on Advanced Composite Materials and Manufacturing Engineering (Cmme2012)*; Trans Tech Publication: Zurich, Switzerland, 2012; pp. 1–430.
3. Wilcox, P.D.; Konstantinidis, G.; Croxford, A.J.; Drinkwater, B.W. *Strategies for Guided Wave Structural Health Monitoring*; AIP: London, UK, 2007; pp. 2961–2981.
4. Raghavan, A.; Cesnik, C.E. Review of Guided-wave Structural Health Monitoring. *Shock Vib. Dig.* **2007**, *39*, 91–114. [[CrossRef](#)]
5. Rose, J.L. Successes and Challenges in Ultrasonic Guided Waves for NDT and SHM. *Mater. Eval.* **2010**, *68*, 494–500.
6. Delrue, S.; Van Den Abeele, K. Detection of defect parameters using nonlinear air-coupled emission by ultrasonic guided waves at contact acoustic nonlinearities. *Ultrasonics* **2015**, *63*, 147–154. [[CrossRef](#)]
7. Clarke, T.; Cawley, P.; Wilcox, P.D.; Croxford, A.J. Evaluation of the damage detection capability of a sparse-array guided-wave SHM system applied to a complex structure under varying thermal conditions. *IEEE Trans. Ultrason. Ferroelectr. Freq. Control* **2009**, *56*, 2666–2678. [[CrossRef](#)] [[PubMed](#)]
8. Cawley, P. Practical Guided Wave Inspection and Applications to Structural Health Monitoring. In Proceedings of the 5th Australasian Congress on Applied Mechanics, Brisbane, Australia, 10–12 December 2007; Martin, V., Faris, A., Daniel, B., Griffiths, J., Hargreaves, D., McAree, R., Meehan, P., Tan, A., Eds.; Engineers Australia: Brisbane, Australia, 2007; pp. 12–21.
9. Steigmann, R.; Iftimie, N.; Savin, A.; Sturm, R. Wind Turbine Blade Composites Assessment Using Non-Contact Ultrasound Method. *J. Clean Energy Technol.* **2016**, *4*, 440–443. [[CrossRef](#)]

10. Raišutis, R.; Jasiūnienė, E.; Žukauskas, E. Ultrasonic NDT of wind turbine blades using guided waves. *Ultrasound Ultragas* **2008**, *63*, 7–11.
11. Jasiūnienė, E.; Raišutis, R.; Šliteris, R.; Voleišis, A.; Jakas, M. Ultrasonic NDT of wind turbine blades using contact pulse-echo immersion testing with moving water container. *Ultragarsas (Ultrasound)* **2008**, *63*, 28–32.
12. Nam, M. Application of Phased Array Ultrasonic Testing to Detect Delamination for Wind Turbine Blade. *J. Wind Energy* **2018**, *9*, 33–42.
13. Bai, Z.; Chen, S.; Jia, L.; Zeng, Z. Phased array ultrasonic signal compressive detection in low-pressure turbine disc. *NDT E Int.* **2017**, *89*, 1–13. [[CrossRef](#)]
14. Chady, T. Wind Turbine Blades Inspection Techniques. *Prz. Elektrotech.* **2016**, *1*, 3–6. [[CrossRef](#)]
15. Willey, C.L.; Simonetti, F.; Nagy, P.B.; Instanes, G. Guided wave tomography of pipes with high-order helical modes. *NDT E Int.* **2014**, *65*, 8–21. [[CrossRef](#)]
16. Løvstad, A.; Cawley, P. The reflection of the fundamental torsional guided wave from multiple circular holes in pipes. *NDT E Int.* **2011**, *44*, 553–562. [[CrossRef](#)]
17. Leinov, E.; Lowe, M.J.S.; Cawley, P. Investigation of guided wave propagation and attenuation in pipe buried in sand. *J. Sound Vib.* **2015**, *347*, 96–114. [[CrossRef](#)]
18. Sharma, A.; Sharma, S.; Sharma, S.; Mukherjee, A. Ultrasonic guided waves for monitoring corrosion of FRP wrapped concrete structures. *Constr. Build. Mater.* **2015**, *96*, 690–702. [[CrossRef](#)]
19. Lu, Y.; Li, J.; Ye, L.; Wang, D. Guided waves for damage detection in rebar-reinforced concrete beams. *Constr. Build. Mater.* **2013**, *47*, 370–378. [[CrossRef](#)]
20. Rathod, V.T.; Roy Mahapatra, D. Ultrasonic Lamb wave based monitoring of corrosion type of damage in plate using a circular array of piezoelectric transducers. *NDT E Int.* **2011**, *44*, 628–636. [[CrossRef](#)]
21. Mustapha, S.; Ye, L. Propagation behaviour of guided waves in tapered sandwich structures and debonding identification using time reversal. *Wave Motion* **2015**, *57*, 154–170. [[CrossRef](#)]
22. Putkis, O.; Dalton, R.P.; Croxford, A.J. The anisotropic propagation of ultrasonic guided waves in composite materials and implications for practical applications. *Ultrasonics* **2016**, *65*, 390–399. [[CrossRef](#)]
23. Castaings, M.; Singh, D.; Viot, P. Sizing of impact damages in composite materials using ultrasonic guided waves. *NDT E Int.* **2012**, *46*, 22–31. [[CrossRef](#)]
24. Raišutis, R.; Kažys, R.; Žukauskas, E.; Mažeika, L. Ultrasonic air-coupled testing of square-shape CFRP composite rods by means of guided waves. *NDT E Int.* **2011**, *44*, 645–654. [[CrossRef](#)]
25. Deng, Q.; Yang, Z. Propagation of guided waves in bonded composite structures with tapered adhesive layer. *Appl. Math. Model.* **2011**, *35*, 5369–5381. [[CrossRef](#)]
26. Masserey, B.; Raemy, C.; Fromme, P. High-frequency guided ultrasonic waves for hidden defect detection in multi-layered aircraft structures. *Ultrasonics* **2014**, *54*, 1720–1728. [[CrossRef](#)]
27. Puthillath, P.; Rose, J.L. Ultrasonic guided wave inspection of a titanium repair patch bonded to an aluminum aircraft skin. *Int. J. Adhes. Adhes.* **2010**, *30*, 566–573. [[CrossRef](#)]
28. Wu, H.C.; Gupta, N.; Mylavarapu, P.S. Blind multiridge detection for automatic nondestructive testing using ultrasonic signals. *IEEE Trans. Ultrason. Ferroelectr. Freq. Control* **2006**, *53*, 1902–1911. [[CrossRef](#)]
29. Satyanarayan, L.; Bharath Kumaran, K.; Krishnamurthy, C.V.; Balasubramaniam, K. Inverse method for detection and sizing of cracks in thin sections using a hybrid genetic algorithm based signal parametrisation. *Theor. Appl. Fract. Mech.* **2008**, *49*, 185–198. [[CrossRef](#)]
30. Tiwari, K.A.; Raisutis, R.; Samaitis, V. Hybrid Signal Processing Technique to Improve the Defect Estimation in Ultrasonic Non-Destructive Testing of Composite Structures. *Sensors* **2017**, *17*, 2858. [[CrossRef](#)]
31. Tiwari, K.A.; Raisutis, R. Post-processing of ultrasonic signals for the analysis of defects in wind turbine blade using guided waves. *J. Strain Anal. Eng. Des.* **2018**. [[CrossRef](#)]
32. Tiwari, K.A.; Raisutis, R. Identification and Characterization of Defects in Glass Fiber Reinforced Plastic by Refining the Guided Lamb Waves. *Materials* **2018**, *11*, 1173. [[CrossRef](#)]
33. Yadav, A.K.; Roy, R.; Kumar, A.P.; Kumar, C.S.; Dhakad, S.K. De-noising of ultrasound image using discrete wavelet transform by symlet wavelet and filters. In Proceedings of the 2015 International Conference on Advances in Computing, Communications and Informatics (ICACCI), Kochi, India, 10–13 August 2015; pp. 1204–1208.
34. Dragomiretskiy, K.; Zosso, D. Two-Dimensional Variational Mode Decomposition. In *Lecture Notes in Computer Science*; Springer: Berlin/Heidelberg, Germany, 2015; pp. 197–208.

35. Wan, J.; Ren, L.; Zhao, C. Image Feature Extraction Based on the Two-Dimensional Empirical Mode Decomposition. In Proceedings of the 2008 Congress on Image and Signal Processing, Sanya, China, 27–30 May 2008; pp. 627–631.
36. Swamy, G.; Baskaran, G.; Balasubramaniam, K. A point source correlation technique for automatic discontinuity identification and sizing using time of flight diffraction. *Mater. Eval.* **2005**, *63*, 425–429.
37. Tiwari, K.A.; Raisutis, R.; Samaitis, V. Signal processing methods to improve the Signal-to-noise ratio (SNR) in ultrasonic non-destructive testing of wind turbine blade. *Procedia Struct. Integr.* **2017**, *5*, 1184–1191. [[CrossRef](#)]
38. Kumar, H.P.; Srinivasan, S. Performance analysis of filters for speckle reduction in medical polycystic ovary ultrasound images. In Proceedings of the 2012 Third International Conference on Computing, Communication and Networking Technologies (ICCCNT'12), Karur, India, 26–28 July 2012; pp. 1–5.
39. Abbate, A.; Koay, J.; Frankel, J.; Schroeder, S.C.; Das, P. Signal detection and noise suppression using a wavelet transform signal processor: Application to ultrasonic flaw detection. *IEEE Trans. Ultrason. Ferroelectr. Freq. Control* **1997**, *44*, 14–26. [[CrossRef](#)]
40. Rodriguez, M.A.; San Emeterio, J.L.; Lazaro, J.C.; Ramos, A. Ultrasonic flaw detection in NDE of highly scattering materials using wavelet and Wigner-Ville transform processing. *Ultrasonics* **2004**, *42*, 847–851. [[CrossRef](#)]
41. Yu, G.; Wang, X. Ultrasonic signal processing using wavelet transform for automatic rail defect detection. In Proceedings of the 2016 International Forum on Management, Education and Information Technology Application, Guangdong, China, 30–31 January 2016; Kim, Y.H., Ed.; Atlantis Press: Paris, France, 2016; pp. 678–681.
42. Priya, K.D.; Rao, G.S.; Rao, P.S.V.S. Comparative Analysis of Wavelet Thresholding Techniques with Wavelet-wiener Filter on ECG Signal. *Procedia Comput. Sci.* **2016**, *87*, 178–183. [[CrossRef](#)]
43. Jaffery, Z.; Ahmad, K. Performance Comparison of Wavelet Threshold Estimators for ECG Signal Denoising. In Proceedings of the 2010 International Conference on Advances in Recent Technologies in Communication and Computing (ARTCom), Kottayam, India, 16–17 October 2010; pp. 248–251.
44. Jasim Hussein, N.; Hu, F.; He, F. Multisensor of thermal and visual images to detect concealed weapon using harmony search image fusion approach. *Pattern Recognit. Lett.* **2017**, *94*, 219–227. [[CrossRef](#)]
45. Luo, X.; Bhakta, T. Estimating observation error covariance matrix of seismic data from a perspective of image denoising. *Comput. Geosci.* **2017**, *21*, 205–222. [[CrossRef](#)]
46. Donoho, D.L.; Johnstone, I.M. Ideal Spatial Adaptation by Wavelet Shrinkage. *Biometrika* **1994**, *81*, 425. [[CrossRef](#)]
47. Johnstone, I.M.; Silverman, B.W. Wavelet Threshold Estimators for Data with Correlated Noise. *J. R. Stat. Soc. Ser. B (Stat. Methodol.)* **2002**, *59*, 319–351. [[CrossRef](#)]
48. Elfouly, F.; Mahmoud, M.; Dessouky, M.; Deyab, S. Comparison Between Haar and Daubechies Wavelet Transformions on Fpga Technology. *World Acad. Sci. Eng. Technol.* **2014**, *6*, 417–422.
49. Raisutis, R.; Kazys, R.; Mazeika, L.; Zukauskas, E.; Samaitis, V.; Draudviliene, L.; Vladisauskas, A. An Adjustment-Free NDT Technique for Defect Detection in Multilayered Composite Constructions Using Ultrasonic Guided Waves. *Int. J. Struct. Stab. Dyn. Feedback* **2014**, *14*, 1440025. [[CrossRef](#)]
50. Tiwari, K.A.; Raisutis, R.; Mazeika, L.; Samaitis, V. 2D Analytical Model for the Directivity Prediction of Ultrasonic Contact Type Transducers in the Generation of Guided Waves. *Sensors* **2018**, *18*, 987. [[CrossRef](#)]
51. Su, Z.; Ye, L.; Lu, Y. Guided Lamb waves for identification of damage in composite structures: A review. *J. Sound Vib.* **2006**, *295*, 753–780. [[CrossRef](#)]
52. Alleyne, D.; Cawley, P. A two-dimensional Fourier transform method for the measurement of propagating multimode signals. *J. Acoust. Soc. Am.* **1991**, *89*, 1159–1168. [[CrossRef](#)]
53. Raišutis, R.; Kažys, R.; Žukauskas, E.; Mažeika, L.; Vladišauskas, A. Application of ultrasonic guided waves for non-destructive testing of defective CFRP rods with multiple delaminations. *NDT E Int.* **2010**, *43*, 416–424. [[CrossRef](#)]
54. Raišutis, R.; Tumšys, O.; Kažys, R. Development of the technique for independent dual focusing of contact type ultrasonic phased array transducer in two orthogonal planes. *NDT E Int.* **2017**, *88*, 71–80. [[CrossRef](#)]

55. Li, W.; Cho, Y.; Lee, J.; Achenbach, J.D. Assessment of Heat Treated Inconel X-750 Alloy by Nonlinear Ultrasonics. *Exp. Mech.* **2013**, *53*, 775–781. [[CrossRef](#)]
56. Cantrell, J.H.; Yost, W.T. Nonlinear ultrasonic characterization of fatigue microstructures. *Int. J. Fatigue* **2001**, *23*, 487–490. [[CrossRef](#)]



© 2019 by the authors. Licensee MDPI, Basel, Switzerland. This article is an open access article distributed under the terms and conditions of the Creative Commons Attribution (CC BY) license (<http://creativecommons.org/licenses/by/4.0/>).